The Astrophysical Journal, 728:1 (16pp), 2011 February 10 doi:10.1088/0004-637X/728/1/1

THREE-DIMENSIONAL STRUCTURE OF A SOLAR ACTIVE REGION FROM SPATIALLY AND SPECTRALLY RESOLVED MICROWAVE OBSERVATIONS

Samuel D. Tun[1], Dale E. Gary[1], and Manolis K. Georgoulis[2]
[1] Physics Department, New Jersey Institute of Technology, Newark, NJ 07102, USA; sdt4@njit.edu
[2] Research Center for Astronomy and Applied Mathematics Academy of Athens, 4 Soranou Efesiou Street, Athens GR-11527, Greece
Received 2010 October 5; accepted 2010 November 4; published 2011 January 13

ABSTRACT

We report on the structure of the solar atmosphere above active region (AR) 10923, observed on 2006 November 10, as deduced from multi-wavelength studies including combined microwave observations from the Very Large Array (VLA) and the Owens Valley Solar Array (OVSA). The VLA observations provide excellent image quality at a few widely spaced frequencies, while the OVSA data provide information at many intermediate frequencies to fill in the spectral coverage. Images at 25 distinct frequencies are used to provide spatially resolved spectra along many lines of sight in the AR, from which microwave spectral diagnostics are obtained for deducing maps of temperature, magnetic field, and column density. The derived quantities are compared with multiwavelength observations from the *Solar and Heliospheric Observatory* and *Hinode* spacecraft, and with a current-free magnetic field extrapolation. We find that a two-component temperature model is required to fit the data, in which a hot (>2 MK) lower corona above the strong-field plage and sunspot regions (emitting via the gyroresonance process) is overlaid with somewhat cooler (∼1 MK) coronal loops that partially absorb the gyroresonance emission through the free–free (Bremsstrahlung) process. We also find that the extrapolated potential magnetic fields can quantitatively account for the observed gyroresonance emission over most of the AR, but in a few areas a higher field strength is required. The results are used to explore the coronal configuration needed to explain the observations. These results show that the bulk of free–free emission in both radio and X-rays emanates from two loop systems, distinguished by the location of their loop footpoints. We discuss the implications of such comparisons for studies of AR structure when better microwave spectral imaging becomes available in the future.

Key words: Sun: corona – Sun: magnetic topology – Sun: radio radiation

Online-only material: color figures

1. INTRODUCTION

The magnetic pressure dominates over the plasma pressure in the corona, so that the magnetic field controls the distribution of the density and temperature. In addition, the release of magnetic energy is proposed to be the chief mechanism for energy deposition from sub-surface processes into the million-degree corona (Aschwanden 2004, chap. 1). Great effort has been expended toward determining the three-dimensional distribution of the magnetic field, temperature, and density of the corona above solar active regions (ARs) in order to understand magnetic energy storage and subsequent release. Radio observations of the Sun provide a powerful diagnostic of the coronal plasma since they offer a direct measure of the electron temperature (T_e), column emission measure (EM), and, depending on the responsible emission mechanism, the total magnetic field strength ($B_{\rm tot}$) or its component (B_l) along the line of sight (Gary & Hurford 2004). There are two radiation mechanisms that dominate the radio emission of the corona from 1 to 20 GHz: free–free (bremsstrahlung) and gyroresonance emission (White & Kundu 1997). The two mechanisms exhibit easily identifiable spectral behavior if sufficient frequency coverage is available, and the aforementioned physical quantities can be directly obtained from spatially resolved spectra, as will be discussed in Section 3.1.

Zheleznyakov (1962) and Kakinuma & Swarup (1962) independently established, on theoretical grounds, that gyroresonance emission must be responsible for the sunspot-associated emission at centimetric wavelengths. Studies at single or a few widely spaced frequencies confirmed this picture (e.g., Lang & Willson 1980, 1982; Alissandrakis & Kundu 1982; Chiuderi-Drago et al. 1982; Shevgaonkar & Kundu 1985; Gopalswamy et al. 1991; Zlotnik et al. 1996, 1998), while optically thin free–free emission was found to be responsible for the plage associated component at these same wavelengths (Felli et al. 1981; Gary & Hurford 1987). Studies at decimetric wavelengths verified that optically thick free–free emission is responsible for the radiation at these longer wavelengths (Chiuderi Drago et al. 1977; Dulk & Gary 1983; Lang & Willson 1982; Lang et al. 1983), although gyroemission may still contribute somewhat in this regime (Lang et al. 1987a, 1987b; White et al. 1992; Vourlidas et al. 1996). The transition between the dominance of the two mechanisms occurs around 10 cm (Gary & Hurford 1987). At very short centimetric wavelengths (⩽2 cm) the emission is again due to free–free emission but emanates from the chromosphere or transition region (Shevgaonkar & Kundu 1985; Hurford 1986; Gary & Hurford 1987). These single-frequency studies determined that, in general, free–free emission dominates at lower frequencies while gyroresonance emission does so at higher ones. This has implications for the distribution of plasma in height above the AR, since emission observed at higher frequencies emanates from deeper in the corona (lower heights above the photosphere) than the radiation at longer wavelengths.

The two mechanisms exhibit distinct spectral shapes (Gary & Hurford 2004) and spectroscopic analysis of spatially resolved radio data returns model-independent physical parameters. The difficulty in carrying out such studies stems from the lack of instruments able to obtain high-fidelity maps at many closely spaced frequencies. Analysis by Gary & Hurford (1987) with a

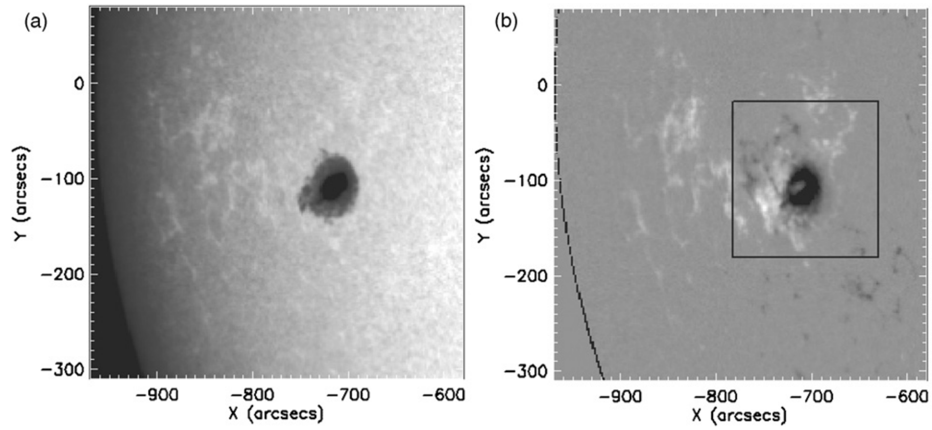

Figure 1. AR 10923 at the photospheric level on 2006 November 10: (a) MDI continuum map and (b) MDI magnetogram with the SOT-SP FOV outlined in black.

potential field extrapolation suggested that the free–free emission at 1.45 GHz originated from the tops of loops connecting the sunspots in the AR. Spectral analysis of source-averaged Owens Valley Solar Array (OVSA) data allowed Lee et al. (1993) to detect a free–free component previously dominated by the gyroresonance signature at higher temperature when their target AR crossed over the limb. Implicit in the geometry of the observations is that the AR had a mega-Kelvin (MK) free–free component overlying a hotter gyroresonance component, which was obscured by the limb when the AR crossed beyond. Gary & Hurford (1994) fit OVSA data with model spectra representative of free–free or gyroemission. In this manner, they produced two-dimensional maps of the T_e, EM, and $B_{\rm tot}$ distributions above their AR as projected onto the sky plane. While most of their averaged spectra conformed to a homogeneous corona model, several spectra were found to have positive slopes in the optically thick part corresponding to low frequencies. In a study using spectra from the sparse frequencies available from the Very Large Array (VLA), Vourlidas et al. (1997) showed that these were best fit by a multi-thermal free–free emission model. However, they too had some spectra that suggested a high positive slope in the optically thick, low-frequency portion which could not be explained by their free–free only models. For those spectra, they concluded that gyroresonance emission was responsible for the radiation at 4.8 GHz and above. In a prior study, Vourlidas & Bastian (1996) found that the soft X-ray and 1.5 GHz VLA observations came from similar structures at the tops of the longest loops connecting the two sunspots in the region, similar to the findings of Gary & Hurford (1987). In their schematic representation of the morphology of the atmosphere as suggested by the analysis, the free–free emission at longer wavelengths comes from greater heights than the sources of the 4.7 and 8.4 GHz emission.

In the present study, we describe the results of combining high-fidelity brightness temperature maps from the VLA with maps providing the high-spectral-resolution capabilities of OVSA. Stacking the maps in frequency allows us to explore the spectra at various lines of sight. The advantage of this approach is that the VLA provides additional spectral points as well as consistency checks for the OVSA data. The latter allows us to study the variations in frequency in greater detail.

We proceed with a description of the observations and supporting data in Section 2. Section 3 reviews the theory, which allows us to obtain physical parameters directly from the spectra. In Section 4, we briefly describe the results of fitting the radio spectra with a single-component model and discuss the shortcomings of such a scheme. We then discuss a two-component model approach that best fits the radio data and use those results in an analysis with the potential field extrapolation. Finally, in Section 5 we discuss the implications of our results for the structure of the corona above the AR.

2. OBSERVATIONS

2.1. Active Region NOAA 10923

Our observations of NOAA active region (AR) 10923 were carried out on 2006 November 10. On this day it was a mature, stable region of alpha configuration located at about S11, E49. The MDI magnetogram shows that at this time the AR consisted of a large, fairly undisturbed negative-polarity sunspot surrounded by a scattered plage of opposite polarity fields, some of them extending to distances ∼100 Mm east of the sunspot (Figure 1). A minor B1 flare event occurred on this day starting at 22:40 UT, but it did not appear to change the loop structure or photospheric magnetic fields as seen in EIT and MDI data. The region was stable until a C3 event at 21:55 on November 12 and developed a light bridge on November 13 (Katsukawa et al. 2007). For our observation day, then, the AR is considered stable enough to perform full-day Earth-rotation synthesis with the radio data.

2.2. Very Large Array Observations

The VLA is a 27-element astronomical interferometer which provides excellent uv coverage at a few frequencies. On this date the VLA observed AR 10923 from 15:18 to 22:46 UT. The data obtained were in left- and right-circular polarizations at 1.41, 4.84, 8.48, and 14.96 GHz (L, C, X, and U bands) while the instrument was in "C" configuration (Thompson et al. 1980). The angular resolution was ∼23″, 6.″6, 3.″7, and 2.″2 at these bands. The data were calibrated using 3C286 and 1543-079 as the amplitude and phase calibrators, respectively. Calibration for the attenuators, necessary for solar observations with the VLA, was carried out by T. Bastian using the latest solar calibration (SOLCAL) data. The maps were CLEANed and self-calibrated using the standard AIPS software. After self-calibration, the rms noise in the maps was ∼1%–3% of the peaks. For this study the maps were combined to form the Stokes I total intensity maps in order to make use of OVSA data, as discussed in the next section.

2.3. Owens Valley Solar Array Observations

OVSA is a seven-element solar-dedicated interferometer which on this date observed the Sun at 39 frequencies from 1.2 to

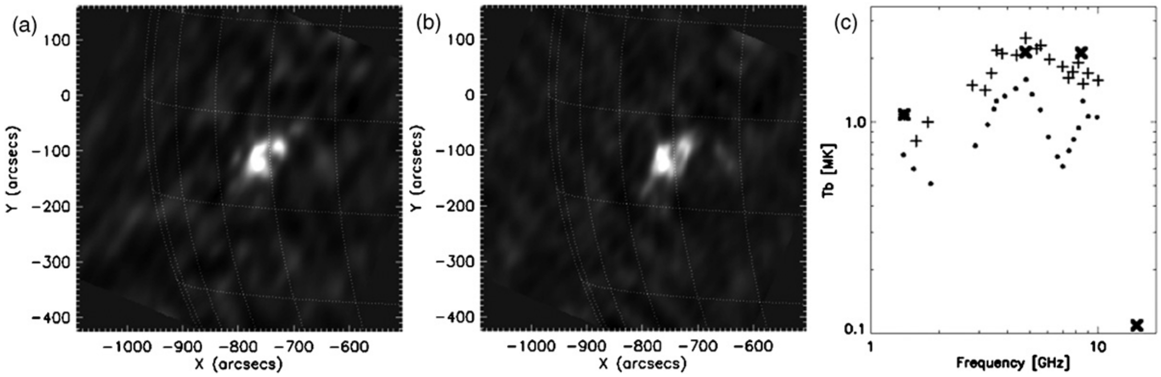

Figure 2. (a) OVSA 4.8 GHz map CLEANed with the revised algorithms. At this stage the T_b levels already match those of the VLA C-band map. (b) Same image after self-calibration. The noise in the maps is reduced while maintaining the structure of the strongest source. (c) Improved spectra from (−760″, −110″), near the T_b peak. The dots represent values from CLEAN maps using the previous versions of the programs, the pluses are the corresponding data points from the self-calibrated maps, and the thick Xs are the VLA data points. Note the amplitude match between both instruments and the improvement in spectral continuity between 5 and 10 GHz.

18 GHz, providing high spectral resolution. After flagging data affected by radio frequency interference, hardware errors, and calibration problems, a total of 21 frequencies remain, ranging from 1.4 to 10 GHz. Twenty minutes of data from around the time of the small B1 flare was excluded, leaving 7 hr 25 minutes of data. We applied the CLEAN algorithm to the OVSA images and convolved the corresponding VLA maps to the OVSA resolution to facilitate comparison. We also developed new IDL-based code to implement the L1 self-calibration algorithm (Schwab 1982; Cornwell & Fomalont 1999) in order to address calibration problems due to atmospheric as well as instrumental effects. The self-calibrated, co-aligned Stokes *I* maps yield good agreement in brightness temperature and general structure with the corresponding VLA maps. The resulting monochromatic maps not only exhibit lower noise, as shown in Figure 2, but also produce smoother spectra when stacked in frequency. While the strong source at the center of the 4.8 GHz map is little affected by the self-calibration, the sidelobe level in the map is greatly reduced. This enables spectral analysis over a region wider than the strong, sunspot-associated source. The rms noise in the self-calibrated maps is 4%–5% of the peak values. The verified amplitude match to the VLA, the improved continuity in frequency, and the low rms noise level make these the best single-frequency OVSA maps ever produced. However, the low number of antennas gives limited *uv* coverage, which in turn results in sidelobe confusion in the synthesized maps. These artifacts are not addressed by self-calibration and persist in the data. This degrades the fidelity of the maps to the level where polarization spectra yield ambiguous results. For this reason a polarization study is not supported by these data. The uncertainties introduced due to our use of the total intensity *I* instead of the *R* and *L* circular polarizations will be addressed in Section 3, before we describe the analysis of the joint data. A comparison with VLA maps at similar frequencies showed that the OVSA phase center was off by about 94″. Since the VLA's phase center is well known, the appropriate shift was found by co-aligning OVSA's 4.8 GHz map to the closest-frequency map from VLA at 4.82 GHz. Applying this fixed shift to all the OVSA maps yielded good spatial agreement at other nearly shared frequencies.

2.4. *Hinode SOT Observations*

The target AR was observed by the suite of instruments aboard the *Hinode* satellite. We obtained Level 2 Solar Optical Telescope (SOT) Spectro-Polarimeter (SP; Lites et al. 2001) vector magnetogram data which had a field of view (FOV) of 102″ × 162″ at 0.″148 × 0.″158 pixel resolution (Figure 1(b)). These data report a maximum (negative) field strength of about 3300 G near the sunspot center. Since the absolute pointing of the SOT observations is not well determined (HSOT-DAG 2009), data from the corresponding MDI magnetogram, whose contours matched very well, were used to co-align the data. The purpose of the magnetograms in our study was to provide the boundary conditions for a nonlinear force-free field (NLFFF) extrapolation of the magnetic field which we could use to compare to the results from the radio data, providing an independent test for the extrapolation. However, after obtaining the extrapolation it was found to be inconsistent with expectations based on EUV data and radio results. It was determined that the small FOV of the instrument did not encompass enough of the positive flux surrounding the sunspot, in particular to the east, and therefore provided inaccurate boundary conditions for a proper extrapolation (see also De Rosa et al. 2009). Therefore, our use of SOT-SP data is limited to using the B_z component to complement MDI data (described next) as a boundary condition for a potential field extrapolation, the details of which will be described in Section 2.6.

2.5. *SoHO MDI/EIT Observations*

EUV and magnetogram data were also available from the EIT (Delaboudinière et al. 1995) and MDI (Scherrer et al. 1995) instruments, respectively, onboard the *Solar and Heliospheric Observatory* (*SoHO*) spacecraft. In this study, the full-disk Fe IX/X 171Å, Fe XII 195Å, and Fe XV 284 Å EUV maps are used qualitatively to check the validity of the extrapolation and the radio results. The full-disk MDI magnetogram has 1.″98 × 1.″98 pixel resolution and provides the B_z component of the photospheric magnetic field. In view of the shortcomings of the aforementioned NLFFF extrapolation, we opted to perform a potential field extrapolation, with the MDI magnetogram providing the surface boundary condition. However, we found that the MDI magnetogram was saturated near the peak of the field which requires correction as discussed next.

2.6. *Potential Field Extrapolation*

The study of coronal magnetic fields is enhanced by the combined analysis of microwave measurements with magnetic field extrapolations. One manner in which the results of radio studies

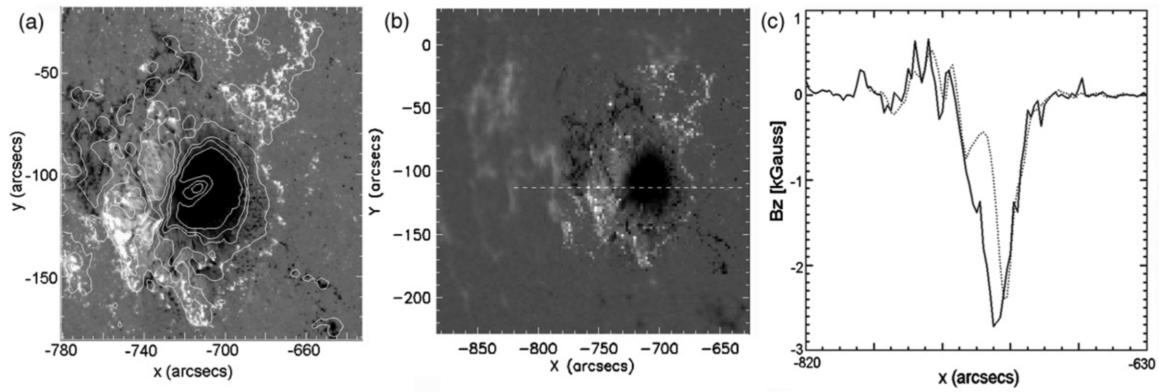

Figure 3. Magnetograms of AR 10923: (a) SOT-SP B_z and FOV overlaid with MDI B_z contours. The saturation in the MDI data shows up as an island of less negative B-field inside the umbra. (b) FOV of the composite MDI/SOT-SP magnetogram used for the extrapolation. (c) Comparison of SP (solid) and MDI (light dots) B_z levels along the dashed line in (b).

can be used is as tests of the extrapolations (White 2004). In this sense, the magnetic field strength in the corona, obtained from radio observations, is compared to the extrapolated field strength. Field extrapolation models can also be used to validate the physical results of the radio analysis. In particular, extrapolations can provide the magnetic field strength $B(h)$ as a function of height h above the photosphere while radio observations provide the electron temperature $T_e(B)$ as a function of magnetic field strength. As a result, combined analysis can potentially provide information on $T_e(h)$.

The choice of appropriate extrapolation technique is open to debate. A general, fairly realistic, but non-unique choice may be the NLFFF extrapolation method that (1) provides an equilibrium solution while relaxing the unrealistic uniform-twist requirement of a linear force-free field (LFFF) extrapolation, and (2) does not preclude very weak electric currents, in the sense that it can asymptotically converge to a current-free, potential solution. NLFFF extrapolations, however, are still an open research topic with different methods applied to the same boundary giving notably different results (Schrijver et al. 2006, 2008; Metcalf et al. 2008). De Rosa et al. (2009), in particular, showed that NLFFF extrapolations applied to data from the SP instrument may provide unreliable estimates of the coronal magnetic field if based on incomplete boundary conditions. One of the proposed treatments in this case was to use vector magnetogram data with a much larger FOV to account for more of the electric currents associated with a given AR. Unfortunately we did not have high-resolution vector magnetograms over wide fields of view available at the time of these observations. Because of the relative simplicity of AR 10923, we expect that the field is approximately potential. For the above reasons, we deliberately choose to use a current-free extrapolation applied to the normal photospheric field component over wide fields of view as the preferred extrapolation method for this study. The comparison of the B_{tot} values inferred by radio observations to the well-known, unique potential-field solution will reveal the areas where strong electric currents persist, thus forcing the observational and extrapolated B_{tot} to disagree, while also showing the areas where weak or absent electric currents allow observed and extrapolated magnetic field values to reasonably agree with each other.

2.6.1. *Boundary Conditions*

For our potential-field extrapolation, we require a sizable patch of the solar photospheric line-of-sight magnetic field from the *SoHO*/MDI magnetogram enclosing AR 10923. For the extrapolation we (1) calculate the heliographic plane corresponding to our FOV (Gary & Hagyard 1990), and (2) interpolate the cosine-corrected normal magnetic field component on this plane. Before performing the above calculations, however, we make an effort to improve the realism of our boundary condition by treating the saturation present in the *SoHO*/MDI data. Saturation in the MDI magnetogram can be seen as an island of less negative flux within the umbra in the MDI contours overlaid on the SOT-SP B_z map in Figure 3(a). The SP magnetogram, derived from spectral polarimetry, is less saturated but as mentioned above its FOV only covers the central region of the AR. After verifying that both instruments measured nearly equivalent magnetic flux levels in locations away from the saturation area (Figure 3(c)), which justifies combining the data sets, we construct a composite MDI-SP magnetogram by embedding the spatially rescaled SP B_z map into the corresponding field of view in the MDI magnetogram. We then use a section of the combined magnetogram large enough to encompass all of the prominent magnetic flux of the AR (Figure 3(b)). We note that De Rosa et al. (2009) used a similar approach to improve the boundary conditions for their extrapolations.

2.6.2. *Extrapolation Method*

To implement our potential extrapolation, we use the Green's functions method as implemented by Schmidt (1964) on Cartesian geometry (see also Georgoulis & LaBonte 2007). Schmidt's (1964) method gives an exact solution, providing potential fields and subsequent zero electric currents up to machine accuracy. The method is much more accurate than the potential (or LFFF) extrapolation techniques relying on fast Fourier transforms (Alissandrakis 1981) but, in return, it is much more computationally intensive. We took this expense, nevertheless, as we need the accuracy to precisely pinpoint possible discrepancies between the function $B(h)$ as estimated by radio observations and the extrapolated $B(h)$, without concern for numerical uncertainties in the extrapolation. Our extrapolation explicitly ignores electric currents, so observed discrepancies should indicate either uncertainties in the observationally inferred $B(h)$ or areas where the potential approximation breaks down, meaning that magnetic field lines are notably distorted by the existence and action of local electric currents. Figure 4 displays sample field lines from the resulting extrapolation overlaid on the EIT 171 Å and XRT Al-med maps to demonstrate general agreement between the model and the location of sources from observations.

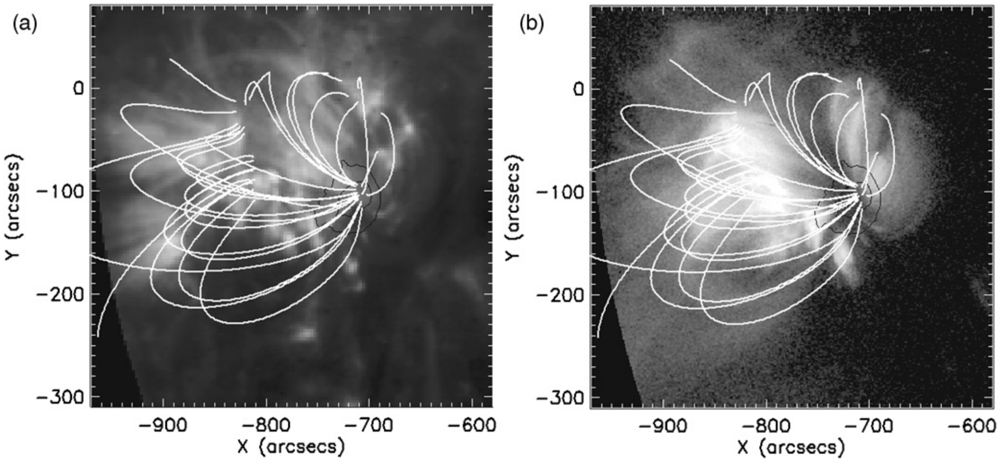

Figure 4. Selected field lines from the potential field extrapolation overlaid on (a) EIT 171 Å and (b) XRT Al-med maps. The location of the field lines generally agrees with the location and shape of the EUV and soft X-ray sources observed. The umbral and penumbral boundaries are outlined in black.

3. RADIO SPECTRAL DIAGNOSTICS AND THE USE OF STOKES *I* DATA

3.1. Radio Spectral Diagnostics

We now briefly review how the physical parameters of electron temperature (T_e), column emission measure (EM), and total magnetic field strength ($B_{\rm tot}$) are obtained from analysis of radio spectra. We discuss the general results relevant to this work and refer the interested reader to the review by Gary & Hurford (2004) and references therein for greater details. Free–free radio emission arises from distant Coulomb interactions between free electrons and ions in the coronal plasma. Gyroresonance emission is a plasma resonance mechanism due to the gyration of electrons around magnetic fields. Because the mechanisms differ in the manner in which they emit, their spectra are different and easily identifiable.

Irrespective of emission mechanism, the solution to the radiative transfer equation for an isolated, homogeneous source (Dulk 1985) is

$$T_b \approx T_e(1 - e^{-\tau}), \qquad (1)$$

where, T_b is the brightness temperature, essentially the surface brightness of an equivalently hot black body, in units of temperature. The optical depth τ is a measure of the absorption and includes most of the physics in the equation. When $\tau \gg 1$, $T_b \simeq T_e$ and the source is optically thick. When $\tau \ll 1$, then $T_b \simeq \tau T_e$ and the source is optically thin. The two regions for a typical spectrum are marked in Figure 5(a), which is a modified version of Figure 4 from Gary & Hurford (1994). It is clear that T_e can be read directly from the optically thick (flat) portion of the spectrum. The two regimes are separated by the condition $\tau = 1$ and it is at this circumstance that we can obtain the other physical parameters.

The optical depth for free–free emission from plasma under typical coronal conditions is given by Dulk (1985):

$$\tau \approx 0.21\nu^{-2}T_e^{-3/2}\int n_e^2 dl, \qquad (2)$$

where n_e is the electron density, ν is the observing frequency, and the integral is taken along the line of sight. The optical depth is proportional to ν^{-2}, which makes the optically thin T_b slope easily identifiable. When $\tau = 1$ the above equation can be rearranged to give

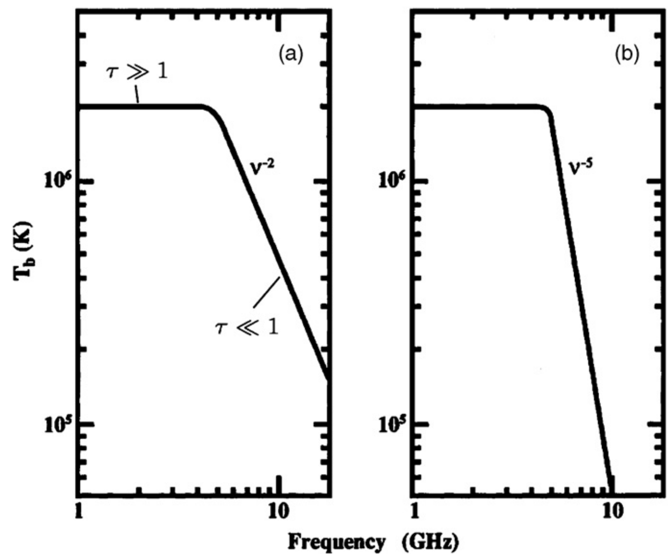

Figure 5. Expected T_b spectra for a homogeneous corona: (a) free–free spectrum with the optically thick and thin regimes labeled, and (b) gyroresonance spectrum with a representative high-frequency slope of ν^{-5}, which may theoretically be as steep as ν^{-10} (adapted from Gary & Hurford 1994).

$$\int n_e^2 dl = 4.8\nu_{\tau=1}^2 T_e^{3/2} {\rm cm}^{-5} = {\rm EM}, \qquad (3)$$

where EM is the column emission measure. The value of $\nu_{\tau=1}$ is also read directly from the spectrum.

Gyroresonance emission is a plasma resonance phenomenon whose optical depth depends on n_e, T_e, ν, the magnetic field strength, gradient, and orientation. While the optical depth along the line of sight is rather sensitive to the angle between the magnetic field and the line of sight, the main condition for the resonance is that $\nu \approx s\nu_B$, where $\nu_B = 2.8 \times 10^6 B_{\rm tot}$. Here, ν_B is the electron gyrofrequency and s is the harmonic number, an integer. The variance of $B_{\rm tot}$ along the line of sight produces a spectrum like the one shown in Figure 5(b). At sufficiently high frequencies, the magnetic fields required to match the resonance condition are no longer in the corona and the brightness temperature begins to drop rapidly to chromospheric temperatures. The frequency at which the spectrum begins to

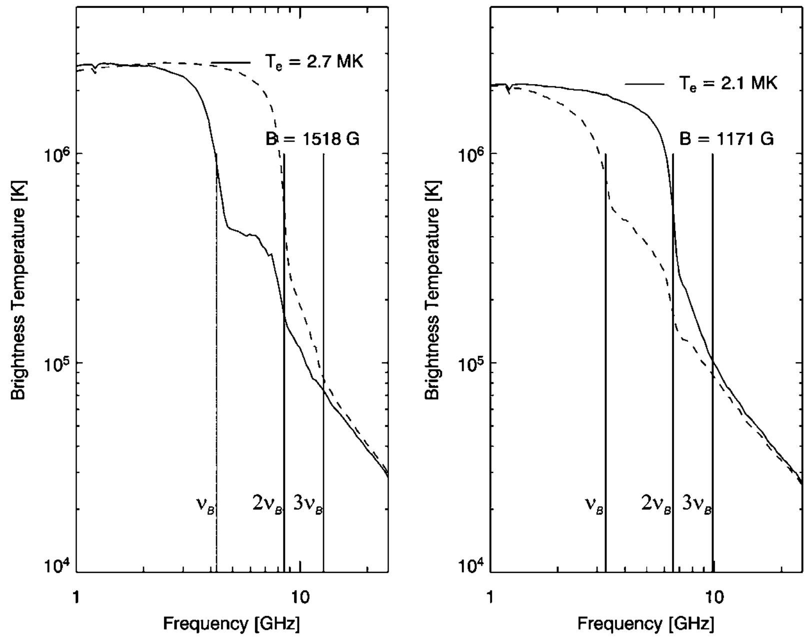

Figure 6. T_b spectra for *R* (solid) and *L* (dashed) circular polarizations along two different lines of sight in an AR coronal model (Mok et al. 2005). The model was sampled with an FASR-like instrument with excellent sky sampling at 100 frequencies from 1 to 24 GHz, resulting in exceptional detail. The spectra become optically thin at different harmonics, and the ratios between the drops are used to identify the harmonic number. (Source: Gary & Hurford 2004. With kind permission from Springer Science + Business Media: Solar and Space Weather Radiophysics, Chapter 4, Radio Spectral Diagnostics, 2004, page 81, Dale E. Gary & G. J. Hurford, Figure 4.5.)

fall comes from the last optically thick harmonic layer still at coronal temperatures. Because of the similarity in shape of the spectra in Figures 5(a) and (b), we can describe the spectrum by Equation (1), although the turnover in Figure 5(b) is not due to an optical depth effect, but rather reflects the inhomogeneity of temperature with height as the optically thick layer descends from corona to chromosphere. In this case, τ should be understood as merely a model parameter and should not be interpreted as optical depth. For mathematical definiteness, we choose the point where Equation (1) becomes $T_b = T_e(1 - e^{-1})$ as defining the turnover frequency $\nu_{\tau=1}$, just above the break, to define the magnetic field at the base of the corona as

$$B_{\rm tot} = \frac{\nu_{\tau=1}}{2.8 \times 10^6 s}. \quad (4)$$

As with the free–free spectrum, this $\nu_{\tau=1}$ can be read directly from the spectrum. In magnetized plasma, the emission is broken down into two plasma wave modes, which can be observed as opposite circular polarizations. A discussion of the modes and the expected harmonics will be presented in the next section, but in general $s = 2$ for ordinary mode and $s = 2$ or 3 for extraordinary mode. The high frequency slope has a dependence of ν^{-5} to ν^{-10}, but variations in temperature and density will keep the slope shallower than the maximum (Gary & Hurford 1994).

3.2. Inversion of Total Intensity Spectra

Radio emission from both the free–free and gyroresonance mechanisms leaves the corona in one of two magnetoionic modes, the ordinary mode (*o* mode) and the extraordinary mode (*x* mode). They are completely circularly polarized when they leave the source, and they correspond generally to the right (*R*) and left (*L*) circular polarizations (Gelfreikh 2004). Polarization observations of free–free emission may be used to determine the longitudinal component of the magnetic field but the degree of polarization from free–free emission is low ($\leqslant$15%). The sidelobe confusion in OVSA images brings the uncertainties up to or above the polarization signal and such a study cannot be carried out with these data. While the VLA samples the sky much more accurately, the reduced number of frequency points limits its use for spectral studies. Furthermore, analysis of the joint polarization spectra reveals that even at higher frequencies, where gyroemission dominates, the polarized signal's root-2 increase in uncertainty relative to *I* yields results that, while consistent with respect to the expected outcome, do not usefully constrain it. We therefore carry out our analysis with total intensity (Stokes *I*) spectra, where $I = (R + L)/2$. Since the physical information is embedded in the polarized signal and *I* is an observational construct, we must first validate such an approach.

As was mentioned earlier, the different modes may become optically thin at different harmonics. This means that spectra in individual polarizations may turn over at different frequencies. Zheleznyakov (1970) found that the *x*-mode harmonic is an order of magnitude higher than that for the *o* mode except when the angle between the magnetic field and the line of sight is close to 0 or 90 deg. Figure 6 shows simulated spectra of a coronal model presented by Mok et al. (2005). The simulation is from a study for the proposed Frequency-Agile Solar Radiotelescope (FASR) which would have many elements sampling the sky with a high spectral resolution. For this reason the sample spectra in the figure reflect the direct model's spectra quite well and small details are visible. For our purposes here it is sufficient to note the difference in turnover frequencies between the *R* and *L* spectra and that their ratio would allow the harmonic number to be determined.

A number of studies have shown that only the lowest harmonics can play a role in the solar corona (Alissandrakis et al. 1980; Felli et al. 1981; Alissandrakis & Kundu 1982; Zlotnik et al. 1996; White & Kundu 1997; Vourlidas et al. 1997). In general, $s = 2$ for *o* mode and $s = 2$ or 3 for *x*

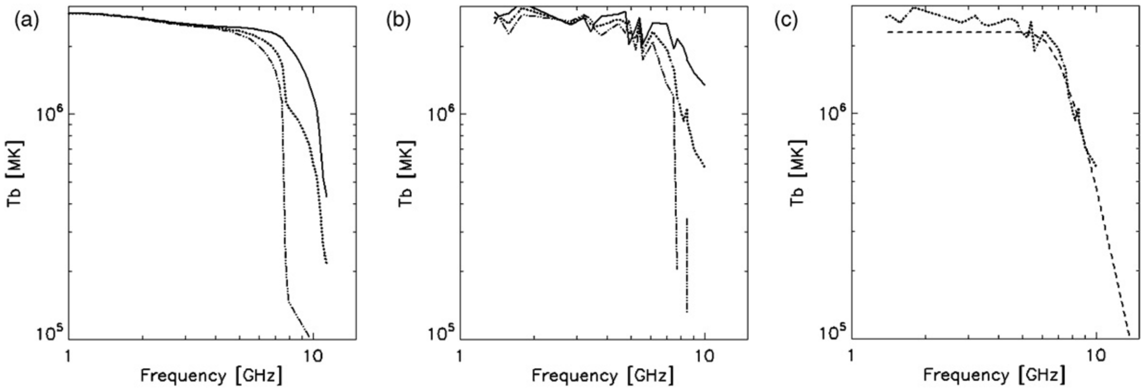

Figure 7. Sample steps in the determination of errors in B_{tot} from the use of I spectra: (a) ideal R and L spectra from the model, sampled at the same frequencies of the VLA-OVSA observations and the I spectrum (dotted), (b) same spectra after 10% noise has been added and the new I (dotted), and (c) the noisy R and L spectra with the fit to the I spectrum (dashed). This last panel shows how closely the fit to the I spectrum follows the spectrum from the lower harmonic, in this case $s = 2$. For this spectra B_{tot} from the fit for $s = 2$ is 1445 G while the value from the model is 1378 G, off by ≈5%.

mode. Only under very special circumstances may the $s = 4$, x-mode layer become optically thick (Holt & Ramaty 1969; Zheleznyakov 1970; Takakura 1972; Ramaty & Petrosian 1972; Vourlidas et al. 1997). The $s = 1$ x-mode emission does not propagate out into the corona because that gyroresonance layer lies beneath its own reflecting point (Zlotnik et al. 1996). The o-mode from this harmonic may propagate but experiments find that even when the $s = 2$ layer above it is optically thin and would allow the emission to go through, the $s = 1$ o-mode is optically thin as well (White 2004).

Since the turnover frequency is used to determine B_{tot} at the base of the corona, we now use the same model from Mok et al. (2005) to determine the error in magnetic field strength as derived from total I spectra instead of R and L. We take the ideal model R and L spectra and sample them only at the frequencies available in our joint VLA-OVSA data. We add random noise at a level that mimics the errors introduced by the incomplete sky sampling, here 10% of the value at each frequency. The I spectrum is formed and fitted with a representative spectrum that has a slope of ν^{-5}. The value of B_{tot} is calculated from $\nu_{\tau=1}$, obtained directly from the model fit, considering $s = 2$ and 3. The actual value of B_{tot} and the correct harmonic are obtained from the uncorrupted spectra and the values are compared. Figure 7 shows an example spectrum illustrating the steps in this process. We find that for differences between the second and third or between the third and fourth harmonics, the errors for B_{tot} from the noisy I spectra and the actual value for the polarization spectrum that corresponds to the lower harmonic are 5%–15%. The I spectrum follows the fall in T_b at the lower harmonic and becomes steeper once the higher harmonic turns over. We conclude that the analysis on I spectra will give B_{tot} values that match those from the lower harmonic within 15%. The problem of determining the proper harmonic from the actual data will be addressed via optical depth calculations using the magnetic field extrapolation.

4. SPECTRAL ANALYSIS AND RESULTS

The joint VLA-OVSA observations sample AR 10923 at 25 frequencies from 1.4 to 14.96 GHz. The maps were resampled to the resolution of the 10 GHz map of 2″.3 × 2″.3 pixels for co-alignment and selection of the FOV. This pixel resolution under-samples only the VLA's U-band map, which has a pixel resolution of 0″.5, and over-samples all the other maps. These maps were averaged over 4 × 4 pixel areas to further reduce noise. The final maps in the data cube consisted of 64 × 64 pixel arrays where each pixel covers a 9″.2 × 9″.2 area.

4.1. Two-component Model

With the OVSA data set improved by the VLA's additional points, and the frequency range doubled, we automated the spectral-fitting method employed by Gary & Hurford (2004), fitting individual spectra with models representing either free–free or gyroresonance emission. The distribution of T_e covers most of the AR and it displays two peaks, one over the region south-east of the sunspot and other one directly over it. While many spectra are fit well with such models, we note that most of the spectra near the sunspot have a positive slope in the optically thick portion, of the same type as Gary & Hurford (2004) found in some of their spectra. For these spectra, an example of which is shown in Figure 8(a), it is obvious that the homogeneous, single-component corona model (dashed line) does not fit the data well.

Gary & Hurford (2004) proposed three possible explanations for their observed positive-slope spectra: (1) a non-thermal electron population, (2) low resolution at low frequencies not being able to resolve all the structure, or (3) a cooler (1 MK) medium overlying a hotter (3 MK) source. On the first point, we reiterate that the radio maps are produced from all day integration of the radio data. In order for the signature of a non-thermal population to appear in such maps, the brightness temperatures reached should be quite high, such as with flares or peculiar, neutral-line sources (Alissandrakis et al. 1993), or the population should be sustained for a large portion of the observation time. As mentioned before, the data around the single, small flare have been excluded from the Earth-rotation synthesis maps and no other significant brightness fluctuations appear in the data. That all the spectra over the strongest photospheric fields, covering an area slightly larger than the sunspot, exhibit the positive-slope feature at varying levels further brings into question the sustainability of such a spatially wide-spread population over a long period of time. The second possibility also seems unlikely to apply to our data set, since our AR is spatially much simpler than the one studied by Gary & Hurford (2004). We find below that the peak in temperature of the free–free component is spatially smooth and occurs well to the east of the region of positive-slope spectra. If the high coronal temperature observed over the sunspot at high frequencies extended to higher heights, it should be reflected

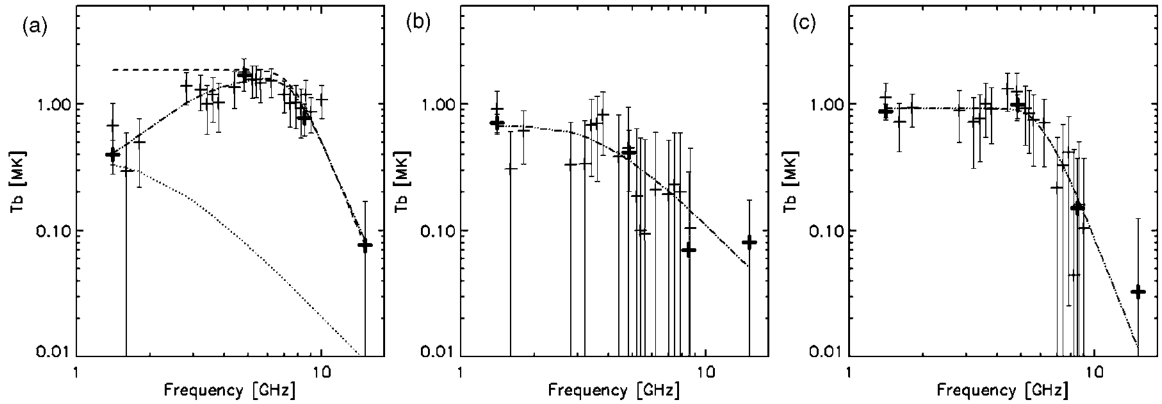

Figure 8. Examples of the fitting algorithm on OVSA (thin + symbols) and VLA (thick + symbols) spectra with error bars: (a) a two-component model best follows this spectrum. The total T_b from Equation (5) is shown in dash-dot-dot line, the gyroresonance component dashed, and the free–free component dotted, (b) a spectrum that was best fit by a homogeneous free–free emission model, and (c) one fit best by a homogeneous gyroresonance emission model.

in a separate, if reduced, free–free (low-frequency) temperature peak at that location. Such a feature is not seen. While these arguments are qualitative, they cast doubt on the viability of the first two solutions for explaining the distribution of positive-slope spectra.

The third possibility, a cooler component overlying a hotter one, seems to be supported by the results of the spectral studies mentioned in the introduction. In accordance with the results of the single or sparse frequency studies discussed there, free–free emission must dominate at low frequencies while gyroemission takes over at higher ones. To explore this possibility, we fit the positive-sloped spectra with a two-component model where a hot gyroresonance component underlies a cooler, but still of MK order, free–free component. The model is of the form

$$T_b = T_{e,\mathrm{gyro}}(1 - e^{-\tau_{\mathrm{gyro}}})e^{-\tau_{\mathrm{ff}}} + T_{e,\mathrm{ff}}(1 - e^{-\tau_{\mathrm{ff}}}), \qquad (5)$$

where $\tau_{\mathrm{ff}} = \alpha/\nu^2$ and $\tau_{\mathrm{gyro}} = \beta/\nu^5$, giving the model's free–free component's optically thin portion a frequency dependence of ν^{-2} and the gyroresonance factor one of ν^{-5}. The observing frequencies when the τ parameters become unity are obtained directly from the model fit since then $\nu_{\mathrm{ff},\tau=1} = \alpha^{1/2}$, and $\nu_{\mathrm{gyro},\tau=1} = \beta^{1/5}$. The values of $T_{e,\mathrm{ff}}$ and $T_{e,\mathrm{gyro}}$ are also obtained directly from the fits. We chose this frequency dependence for the gyroresonance component because, as mentioned in Section 3.1, actual observed spectra will have a frequency slope at the shallower end of the expected range. This is because of temperature and density inhomogeneities within the resolution element or along the line of sight (Gary & Hurford 1994). The slope is further reduced by combining the polarization information into the Stokes *I* parameter. In any case, we found that every gyroresonance slope in our data can be adequately fit with such a model.

An example of how well these spectra are fit with such a model is shown in Figure 8(a). The free–free component is optically thick at low frequencies, dominating the T_b spectrum. As the frequency increases the free–free spectrum becomes optically thin ($\tau_{\mathrm{ff}} < 1$) and the gyroresonance component begins to dominate, raising T_b since $T_{e,\mathrm{gyro}} > T_{e,\mathrm{ff}}$. While single-frequency studies have shown that both emission mechanisms have roles in different regions in monochromatic T_b maps, the variation here is along a given line of sight. If a spectrum is best fit by a single component model, the algorithm is allowed to prefer that (Figures 8(b) and (c)). As we will see in the analysis, this reproduces the known results where free–free emission dominates over the plage areas of the AR and that gyroemission is the chief mechanism over the sunspot area. This yields a stratified coronal model.

4.2. Physical Maps

The temperature distributions of the two components plotted over the SP-MDI magnetogram are displayed in Figure 9(a), with the gyroresonance T_e contours in red and the free–free ones in yellow. The gyroresonance component reaches a peak temperature of 2.5 MK while the maximum in the free–free distribution is 1.6 MK. The gyroresonance electron temperatures exhibit a two-peak structure with one peak directly over the B_z peak and the other, higher T_e peak aligned north–south over the region of scattered positive photospheric magnetic flux directly adjacent to the southeast of the sunspot. The free–free T_e distribution has its single peak over a region about 130″ southeast of the sunspot while the entire distribution covers a large area encompassing the photospheric plage region. The spatial arrangement of the two components is in agreement with the well-established influence of free–free emission over the plage areas and of the dominance of gyroresonance emission near the sunspot. We want to emphasize that these distributions were obtained through model fits to spectra corresponding to individual pixels, each fit independent from all others.

Figure 9(b) displays the same elements as in Figure 9(a), now overlaid with a sample of field lines from the potential field extrapolation. In this view, the peak of the free–free temperature distribution is co-located with the tops of loops connecting the central portion of the extended plage to the sunspot. Long field lines reconnect to the negative-polarity sunspot and the legs of these loops are co-located with the distribution of gyroresonance temperatures. These inferences agree with the conclusions of previous studies where the free–free dominated emission from VLA's *L*-band maps comes from loop tops reconnecting sunspots within ARs (Gary & Hurford 1987; Vourlidas et al. 1996) and that gyroresonance dominates when the magnetic field is strongest, near the base of the corona over sunspots. The tops of the loops extending to the *N* of the sunspot do not have a significant radio-derived temperature co-located with them.

The values for the column EM were obtained only for the pixels containing a free–free component, since the equation is valid only for this mechanism. Further constraints were imposed on the pixel selection for this quantity, since the resulting turnover frequency from the model fit is used. The contours

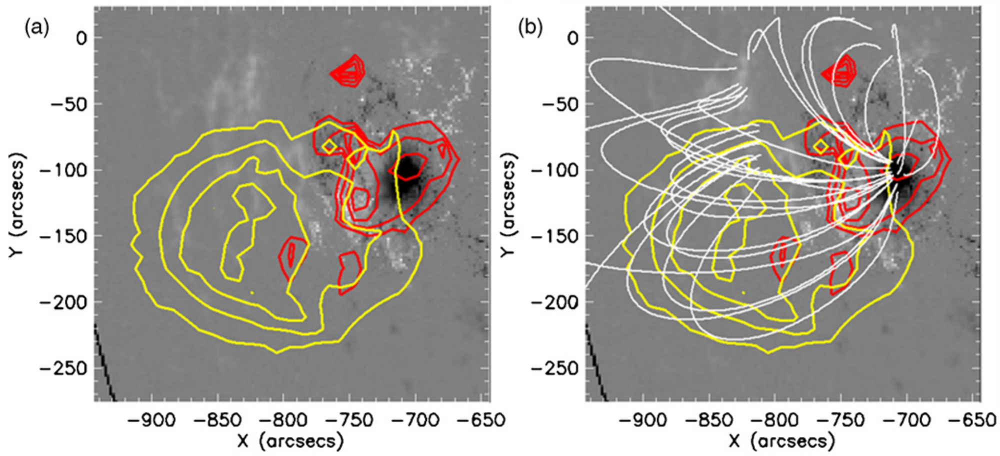

Figure 9. Temperature distributions on the combined SOT-SP/MDI magnetogram: (a) $T_{e,\mathrm{gyro}}$ (off-white) and $T_{e,\mathrm{ff}}$ (dark gray) with levels = [0.3,0.5,0.7,0.8,0.9] × T_{max}, where $T_{\mathrm{max}} = 1.6$ MK for free–free and $T_{\mathrm{max}} = 2.5$ MK for gyroemission and (b) the same contours with representative field lines from the extrapolation (white).
(A color version of this figure is available in the online journal.)

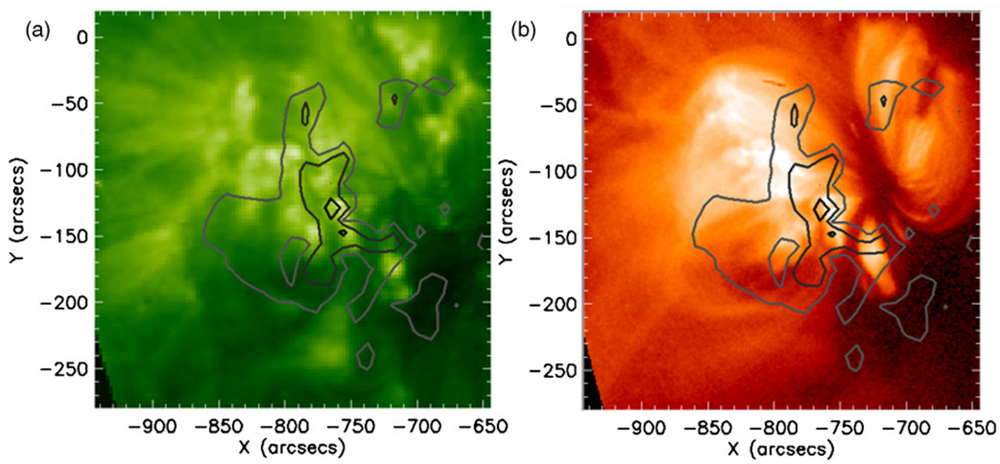

Figure 10. Emission measure levels 20, 60, and 120 × 10^{27} cm^{-5} (gray to black) on (a) EIT's 195 Å map and (b) XRT's C-poly filter map.
(A color version of this figure is available in the online journal.)

for levels 20, 60, and 130 × 10^{27} cm^{-5} are shown on the EIT 195 Å and XRT's C-poly maps in Figure 10. These values are within an order of magnitude of those found by Gary & Hurford (2004). The peak of the EM is outlined in black and overlies what appear to be loop footpoints in EUV and the bottom edge of the brightest emission in X-rays. A comparison with Figure 9 shows that the greatest EM values occur away from the $T_{e,\mathrm{ff}}$ peak. The shape and location of these higher EM values does not appear to match the overall features in the displayed maps, which sample the corona above the AR. We will present a plausible explanation for this distribution in Section 5.1.

Finally, the contours for B_{tot}, of the last optically thick layer along each line of sight for a single harmonic, in this case $s = 3$, are overlaid on the combined SOT-SP/MDI magnetogram in Figure 11(a). The radio spectra turn over due to the rapid drop in temperature from coronal to chromospheric values, so these contours delineate the total magnetic field at the base of the corona. Since the base of the corona is only about 2000 km above the photosphere we expect some correlation between these contours and the photospheric field. Indeed, the radio-derived contours cover the region of strongest photospheric flux of both polarities. The locations of the peaks of the photospheric B_z (white plus sign) and the coronal-base B_{tot} are displaced by ∼28″. The B_{tot} peak lies over the neutral line. Such displacements of coronal to photospheric magnetic field peaks have been encountered in previous studies (Gary & Hurford 1994; Nindos et al. 2000). Figure 11(b) shows the same contours over the MDI continuum map. The location of the coronal-base B_{tot} peak is directly over the umbra/penumbra border.

Since the temperature of the last optically thick layer can be read directly from the spectral fit, we explore the temperature and magnetic field distribution at the base of the corona concurrently. Figure 12(a) outlines $B_{\mathrm{tot}}(s = 3)$ in blue over the T_e distribution scaled in red. The negative-polarity sunspot is outlined by the contours in black while the positive 500 G contour is outlined in light gray. There is a temperature peak over the contours of positive photospheric field, while both hot and cooler temperatures are found within the negative, umbral region. As noted earlier, the peak of the B_{tot} contours lies in between the region of strong negative-polarity and the weaker positive-polarity flux. The letter labels in the map denote regions whose spectra are displayed in Figures 12(b)–(d).

Figure 12(b) shows the spectrum corresponding to the location directly above the absolute T_e peak (location "b"). We see that the high temperature is a consequence of the homogeneous T_e assumption for each component forced to fit to the low-frequency temperatures. However, the value of $\nu_{\tau=1}$, and therefore of B_{tot}, is not affected by this assumption and it is clear that there is an MK signature at the turnover frequency. Figure 12(c) corresponds to location "c," which lies over the

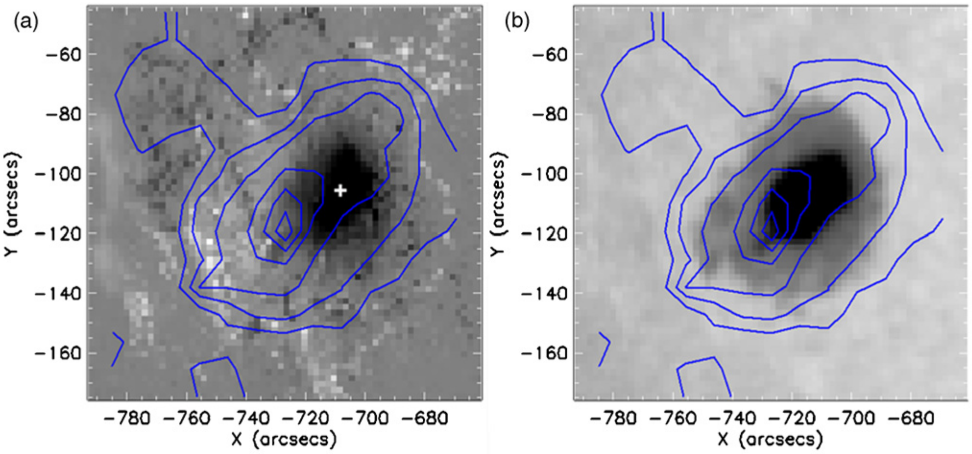

Figure 11. $B_{\rm tot}(s = 3)$ levels 0.3, 0.6, 0.8, 1.0, 1.3, and 1.5 kG on (a) SP/MDI magnetogram with the peak in B_z denoted by the white + and (b) on the MDI continuum map. The $B_{\rm tot}$ peak lies over the neutral line, directly over the umbra–penumbra border.

(A color version of this figure is available in the online journal.)

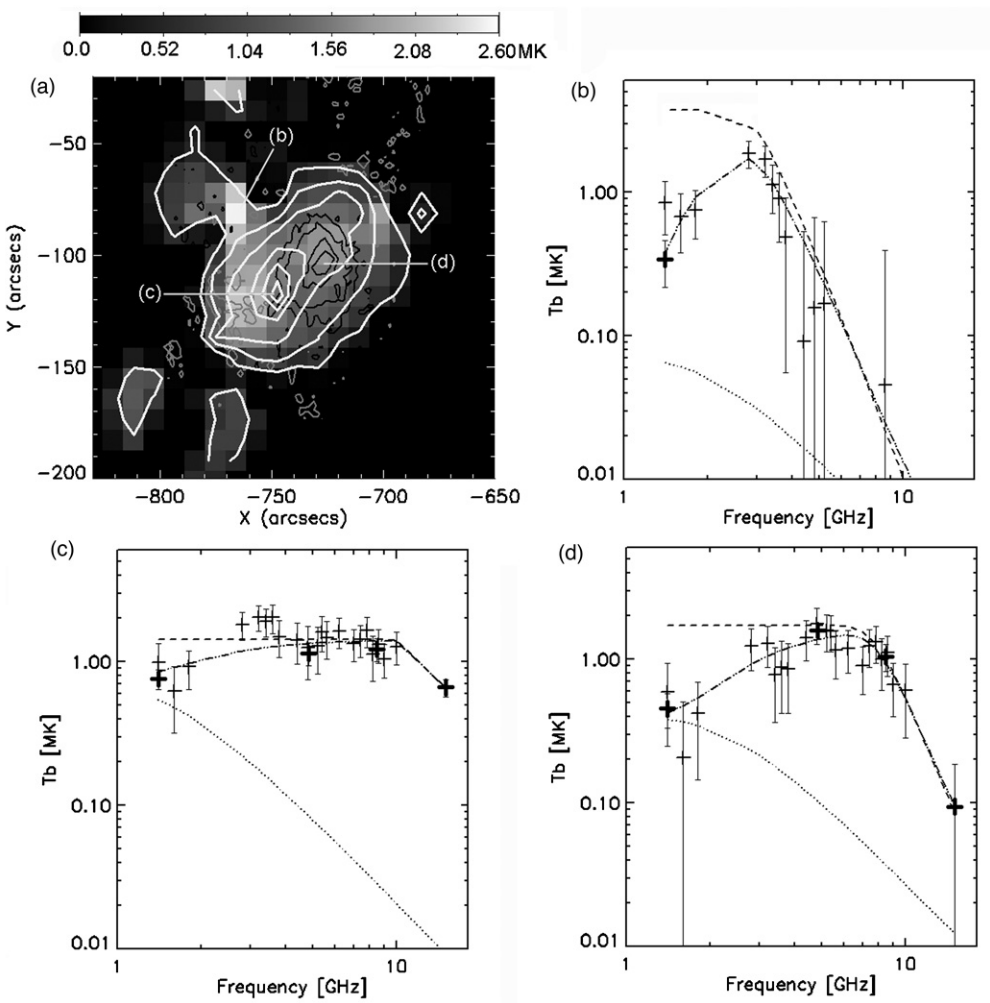

Figure 12. Radio-derived $T_{e,{\rm gyro}}$ and $B_{\rm tot}$ distribution and sample spectra: (a) $B_{\rm tot}$ 0.7, 0.8, 0.9, 1.0, 1.4, and 1.6 kG contours over T_e (gray scale in color bar), with MDI B_z contours for reference, (b) radio spectrum from the location labeled "(b)" in panel (a), corresponding to the $T_{e,{\rm gyro}}$ peak, (c) spectrum corresponding to the $B_{\rm tot}$ peak at location "(c)," and (d) spectrum corresponding to location "(d)," at the photospheric B_z peak.

neutral line and corresponds to the peak of the radio-derived $B_{\rm tot}$ distribution. The turnover frequency obtained from the gyroresonance component corresponds to $B_{\rm tot} = 2.43$, 1.62 kG for $s = 2$ and 3. We quote both the $s = 2$ and 3 values since we do not yet claim to know the appropriate harmonic. Figure 12(d) shows the spectrum over the peak of the photospheric B_z (location "d"). The optically thick temperature of the gyroresonance component is higher than that at location "c," yet the turnover occurs at a lower frequency, resulting in $B_{\rm tot} = 1.33$, 0.89 kG for $s = 2$ and 3. The two-component model reliably fits these spectra, and demonstrates how the displayed distributions are derived.

4.3. Determination of Harmonic Number

As was just mentioned, we do not know the harmonic number for the last optically thick layers. Only high-quality polarization observations, such as those derived from the Mok et al. (2005) model, would exhibit sufficient precision to determine the responsible harmonics directly from the radio spectra by taking the ratio of turnover frequency from both polarization spectra as described in Section 3.2. The available data do not permit this level of separation along any line of sight. This is one of the ambiguities that led us to perform our analysis on I instead of R and L. As was described in that section, the Stokes I spectrum turns over at the same frequency as that of the polarization with the lowest optically thick harmonic, with a small margin of error. The fitting algorithm returns a turnover frequency $\nu_{\tau=1}$ for each line of sight that is adequately fit with a gyroresonance component, from which $B_{\rm tot}$ can be calculated if s is known. The possible values of $B_{\rm tot}$ are limited to harmonics s of the fundamental gyrofrequency, i.e., $s = 2$ and 3, and possibly 4 under coronal conditions. Thus, for a given line of sight, we have only three possible values of $B_{\rm tot}$ corresponding to the three possible harmonic numbers. Since the polarization signature in our data is of insufficient quality to obtain the correct harmonic independently, we turn to the potential field extrapolation to calculate which of these harmonics are optically thick. The extrapolation provides θ, the angle between the magnetic field vector and the line of sight.

The current-free extrapolation was de-rotated from the heliographic plane back into the image plane corresponding to the day's observations. The rotated extrapolation is resampled to the resolution of the radio observations so that there is a direct pixel-to-pixel correspondence in x, y, where each pixel represents a line of sight along z. At each pixel with a gyroresonance component and therefore with three possible values of $B_{\rm tot}$, the extrapolation is searched for the location in z where the values are matched, and the optical depth is calculated at these locations. Since these values correspond to a single turnover frequency, the optically thick layer closest to the observer is the one responsible for the observed emission. By resolving the issue of appropriate harmonic, we are determining the magnetic field strength of the last gyroresonance layer in the corona for each line of sight. The method is applied to all lines of sight independently.

For the calculations of optical depth we require the exact equations since the various approximations often used have been shown to have various problems (Vourlidas et al. 1997). We obtained the full equations for optical depth of the two wave modes from Vourlidas (1996) as derived from the corrected formulae of Melrose & McPhedran (1991). The values of T_e and B are observables obtained directly from the spectrum. The value of θ, the angle between the magnetic field and the line of sight, is obtained from the extrapolation at the matching location for each of the possible values of B. For the electron density n_e an array of values of [8.5, 9, 9.5, 10] $\times 10^9$ cm^{-3}, which covers the range values found from previous studies (i.e., Shevgaonkar & Kundu 1985; Gary & Hurford 1987; Lee et al. 1993), was employed. The studies quoted obtained the higher values for high frequency observations, up to 15 GHz, while the lowest value is from a turnover frequency of 4 GHz. In addition, several workers report that $\tau_{\rm gyro}$ is not as greatly affected by the choice of n_e as by the choice of θ (Vourlidas et al. 1997), so that we are confident that this range of values encompasses realistic values. In our analysis, the differences from using the various densities are minimal, confirming that the results are not very dependent on density. A pixel is set to be optically thick if $\tau > 0.9$ in our calculations.

We first display the results of the optical depth calculations in terms of area coverage. Figure 13 displays the optically thick pixels (white) for both o and x modes for $s = 2$ and 3. The $s = 4$ layer is nowhere optically thick so it is not displayed. The 400 G contour from the radio derived $s = 3$ map is displayed as it outlines the edge of the gyroresonance source. Some MDI contours are also included as a reference. The calculations show the expected structure (White 2004) as follows: there is a window above the sunspot center where only the $s = 2$ x-mode layer is optically thick, the $s = 3$ layer covers a larger area than the $s = 2$ layer because it comes from lower magnetic fields at higher altitude, and the $s = 3$ o-mode layer is optically thick only at particularly inclined angles and so it has a wider window of optically thin pixels over the sunspot center. Figure 14(a) shows the total area covered by optically thick pixels with the same reference contours. The areas where the radio spectral fitting returns a gyroresonance signature, but the calculations do not yield optically thick pixels, are labeled A–D, and can be considered regions where the extrapolation is not consistent with the radio observations. It is interesting that these regions are also the locations of temperature peaks in the gyroresonance T_e distribution, as seen in Figure 14(b). Figure 15 displays spectra from each of the labeled locations A–D. These spectra display a clear gyroresonance signature. Further inspection reveals that the discrepancy occurs because the extrapolation does not contain high enough magnetic field strengths along these lines of sight to match those derived from the radio spectra. While the method shows that the extrapolation is able to match observations along many lines of sight, we now use the T_e distribution to further explore the areas where there is a discrepancy.

4.4. Location of Inferred Coronal Currents and Departure from Potentiality

A comparison of the gyroresonance component's T_e distribution with X-ray data from XRT shows that the peaks in temperature correspond to the footpoints of X-ray loops. In turn, these X-ray loop footpoints lie directly over the penumbra (Figure 16(a)). When considering the map overlays in these figures it is important to keep in mind that the AR is at ∼49E longitude and projection effects will make the forward loop component appear to overlie the leading part of the umbra. Other workers have reported this effect (i.e., Vourlidas et al. 1997 and references therein). The existence of very hot, X-ray emitting plasma, coinciding with the peaks of the gyroresonance temperature at the base of the corona, in regions where the observed magnetic field strength is higher than that in the extrapolation, imply that these are regions with an increased heating function where coronal currents raise the magnetic field above potential state values.

5. IMPLICATIONS FOR THE ATMOSPHERIC STRUCTURE ABOVE AR10923

There are two main results from the model fitting: (1) that the corona, as seen through radio observations, can be modeled as two stratified layers, the lower one of which is dominated by gyroresonance emission while the higher one emits via

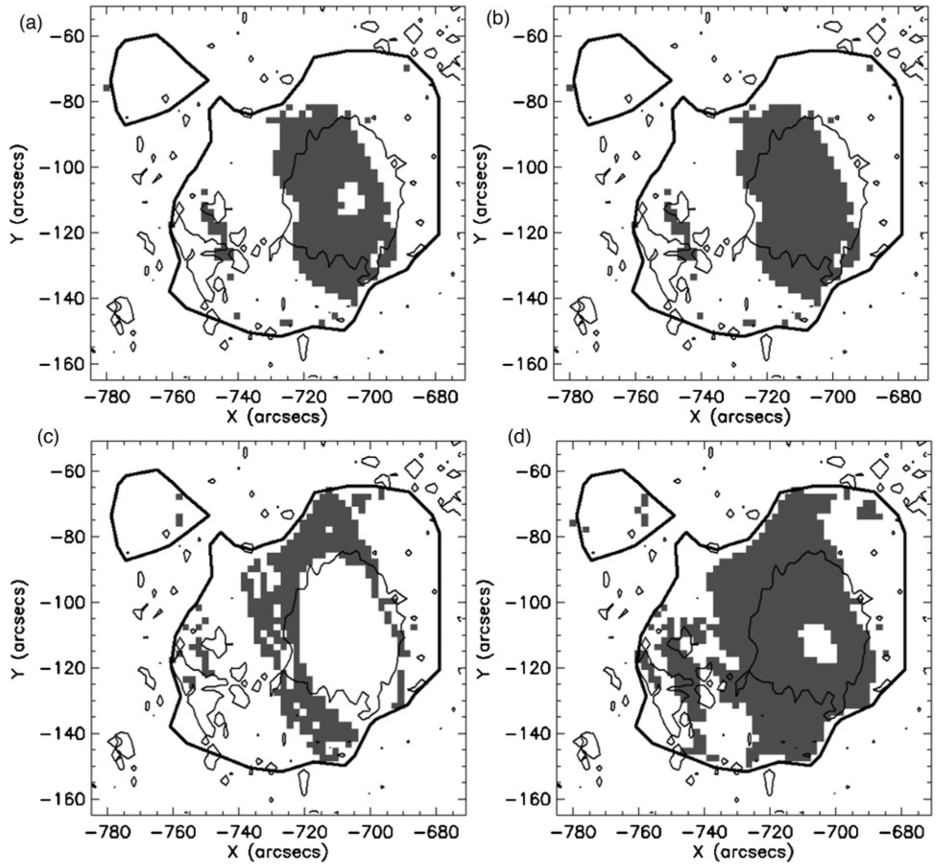

Figure 13. Optically thick lines of sight (gray) for the various gyroresonance layers, as determined from calculations with radio data. The 400 G contour from the radio-derived $s = 3$ $B_{\rm tot}$ (thick black) and the (−600, 500) B_z contours are included for reference (thin black): (a) $s = 2$, *o*-mode, (b) $s = 2$, *x*-mode, (c) $s = 3$, *o*-mode, and (d) $s = 3$, *x*-mode.

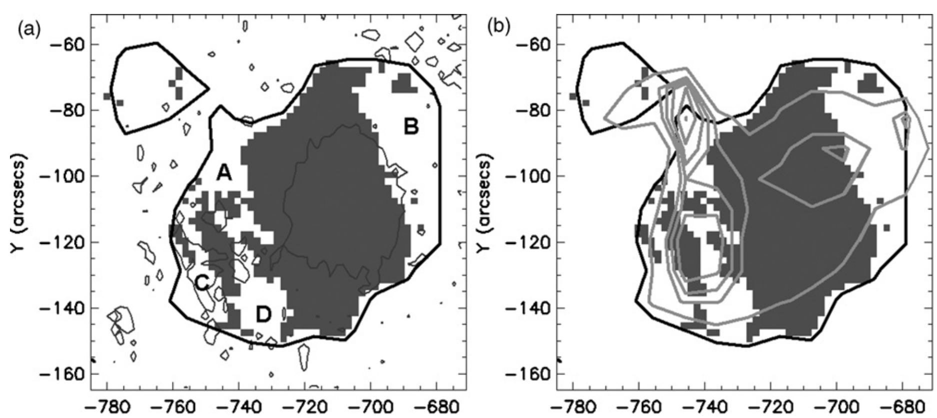

Figure 14. (a) Total area covered by optically thick lines of sight—a combination of pixels in Figure 13, (gray), with other contours as in Figure 14. The areas labeled A–D are regions where the extrapolated B field is too low to match that derived from the radio spectra. (b) Gyroresonance-derived T_e distribution in the same FOV. The locations of the T_e peaks coincide with (A, C, and D) or straddle (B) the regions of discrepancy.

free–free emission, and (2) that the base of the corona is not uniform in temperature nor magnetic field strength. These results can be used in conjunction with other data to explore the three-dimensional configuration of the corona. In the following discussion, we demonstrate the use of our results in obtaining such information.

5.1. Thermal Free–Free Emission in the Corona

While it is not expected that the transition from the gyroresonance to free–free dominated regime is abrupt or co-planar, it provides restrictions on the temperature and density distributions along coronal loops. As we see in Figure 9(b), the free–free emission dominates at the tops of certain loops, and gyroemission appears to take over at the legs or footpoints (Figure 16). Since the free–free emitting loops do not appear different in length or shape from some non-emitting loops in the extrapolation, they must differ in the location of their footpoints. This has consequences for the configuration of the heating function at the base of the corona throughout the entire AR.

Rosner et al. (1978) found that for loops in hydrostatic equilibrium, the temperature maximum is near the loop apex.

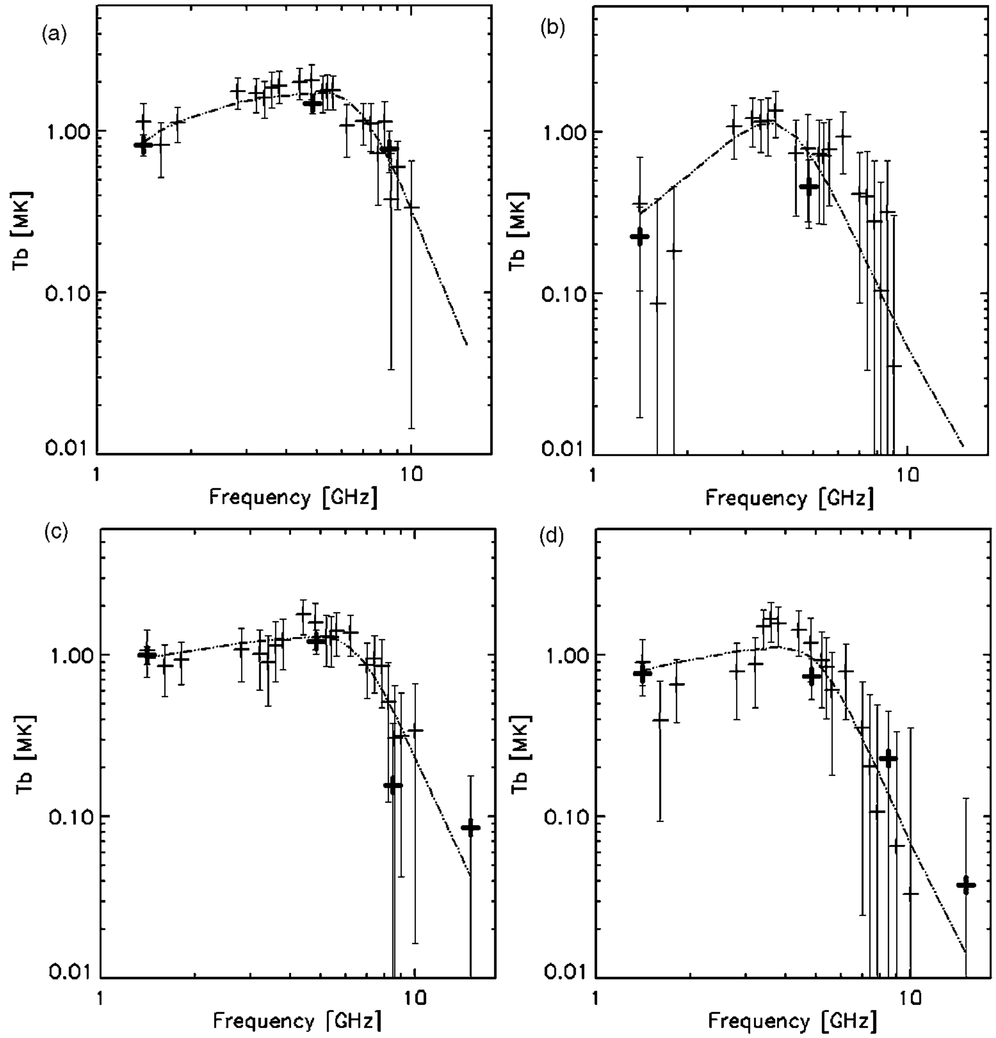

Figure 15. OVSA (+) and VLA (bold +) spectra corresponding to the labeled points in Figure 15(a) along with the fit's two-component model (dashed) and corresponding rms error bars: (a) spectra for location A, (b) location B, (c) location C, and (d) location D.

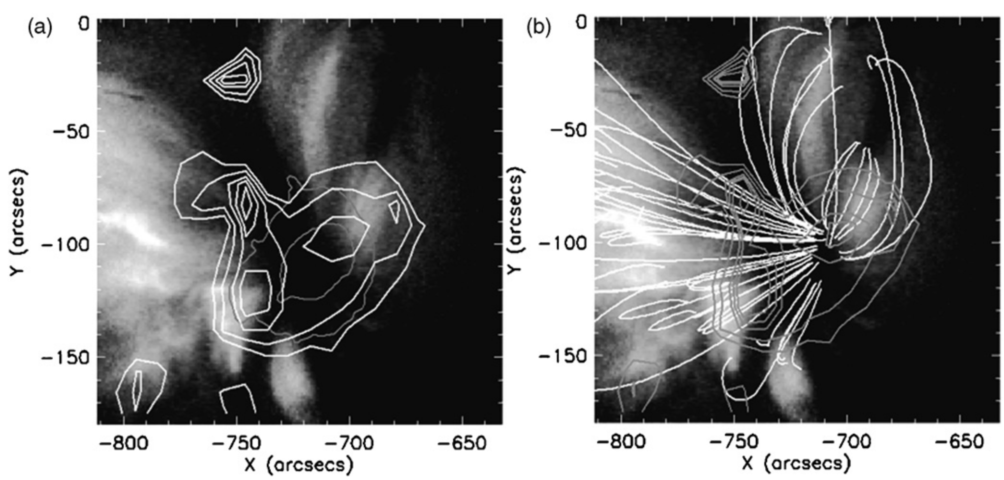

Figure 16. XRT's Al-med filter data overlaid with (a) the white-light umbral and penumbral boundaries (gray) and the gyroresonance T_e (white) and (b) the same T_e (now gray) with matching field lines (white). Field line matching is discussed in Section 5.

Because of the stability of the region and the apparent loop configuration throughout the observation day, we can consider this condition to be a valid approximation for our AR. Based on this assumption we are able to identify two distinct loop systems corresponding to the observed radio and X-ray free–free emission. To match the radio free–free component, we identify and plot those loops whose tops coincide with $T_e > 0.9$ MK (Figure 17(a)). A comparison of these radio loops on the XRT map (Figure 17(b)) shows that, while some of these loops coincide with diffuse X-ray emission, the brightest X-ray

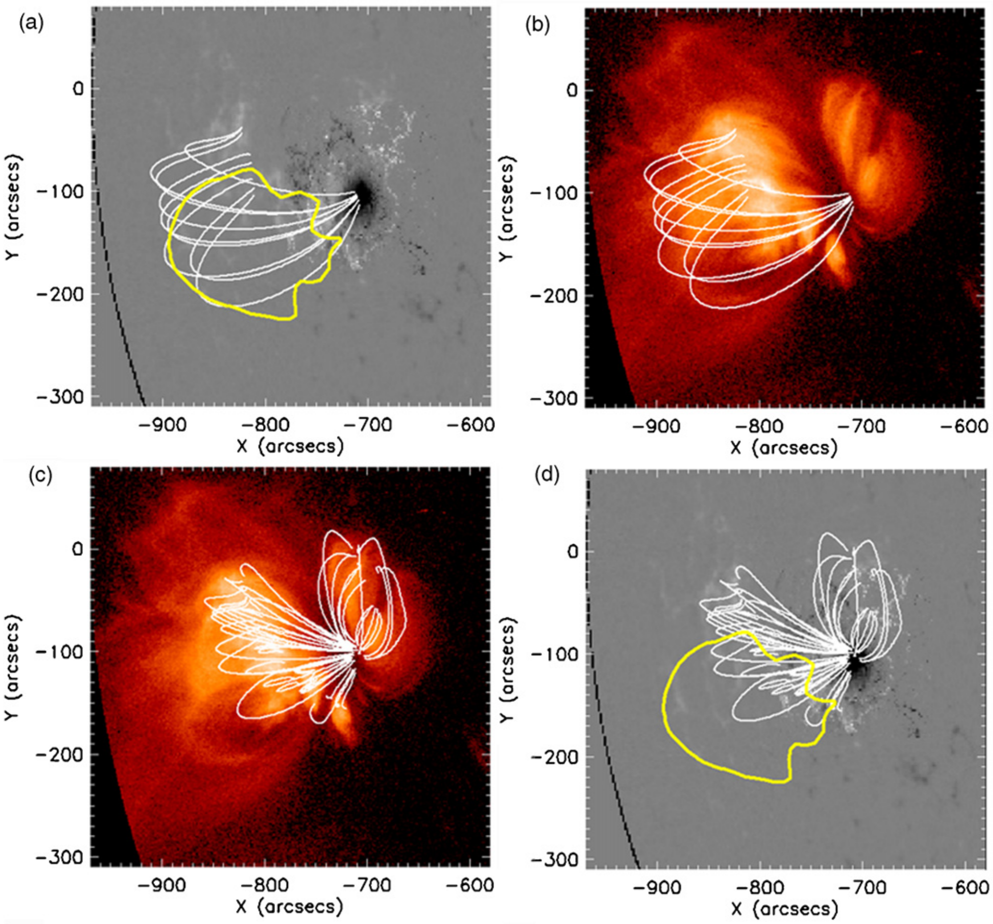

Figure 17. Field line matching to emission source: (a) field lines whose loop tops coincide with radio free–free emission at $T_e > 0.9$ MK (dark gray), (b) the radio source matching field lines overlaid on X-ray data (Al-med) from XRT, (c) field lines with loop tops within the brightest X-ray free–free emission from the same filter, and (d) the X-ray matching field lines overlaid with the same radio T_e distribution as in (a). There is some diffuse cross emission between both loop systems.

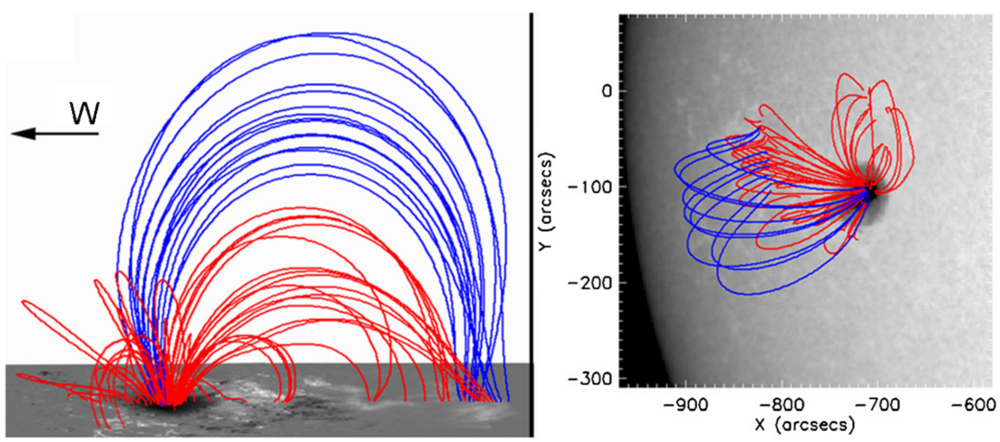

Figure 18. Schematics of the distribution of the X-ray (red) and radio (blue) emitting groups of loops: (a) as seen looking S from solar N and (b) overlaid on the MDI continuum map as observed in the image plane. Note the differences in height and footpoint locations.

signatures lie near their footpoints or legs. Similarly, we identify X-ray emitting loops as those whose tops are co-aligned with the brightest X-ray free–free emission from the Al-med XRT filter (Figure 17(c)). A comparison to the radio T_e distribution (Figure 17(d)) shows that the tops of a few of the longest of these loops lie within the 0.9 MK contour. These comparisons demonstrate that while there is some overlap in emission from both, as would be expected, the bulk of the emission coincides with the loop tops from two different loop systems. Why, then, should the two loop systems be dominated by free–free emission at two different wavelengths?

Having found extrapolation elements with loop tops coincident with radio or X-ray free–free emission, we use the model to create a schematic of the field-line configuration. The cartoon displayed in Figure 18(a) shows the configuration as seen from solar North. Here field lines matching the radio source are in blue and the ones matching the X-ray sources are in red. The field lines responsible for the bulk of the radio free–free

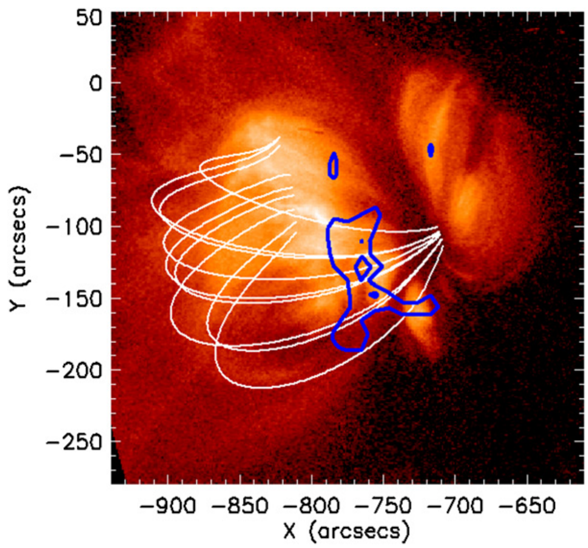

Figure 19. Field lines correlated with free–free radio emission (white) and the derived emission measure distribution levels 60 and 120 × 10^{27} cm^{-5} (gray) on XRT's Al-med filter map.

emission reach greater heights than the X-ray ones. However, there is a multitude of field lines of equal length, not shown here for clarity, that show neither radio nor X-ray emission. The difference, then, must lie in the location of the footpoints and associated heating. Figure 18(b) displays the image-plane view of the two loop systems, showing that the radio loops converge to a point inside the nest made by the X-ray loop footpoints.

As discussed in Section 4.4, the available observations show that the X-ray footpoints overlie the penumbral region so the free–free loops fall within the umbra. This means that the values at the center of the $T_{e,\mathrm{gyro}}$ and B_{tot} distributions correspond to the footpoints of the radio free–free loops. Within the extrapolation, field lines emerging directly from the peak of the photospheric B_z reconnect to the plage N of the sunspot and overlie the dark X-ray corridor extending diagonally to the northeast from the sunspot (see, for example, Figure 17(b)). Many workers have reported the detection of cooler material over sunspot umbrae than in the surrounding corona (i.e., Foukal et al. 1974; Felli et al. 1981; Kundu et al. 1981; Alissandrakis & Kundu 1982). Other results have suggested that umbral loops may extend to higher altitudes and are filled with cooler plasma (Gary & Hurford 1987; Vourlidas et al. 1997). Vourlidas et al. (1997) found that observed polarization in VLA data could be accounted for only if the umbral and penumbral loops formed two distinct systems with different densities and temperatures, heated by varying heating rates at their footpoints. The implication of these results and the one presented in this paper is that the field lines reach a peak temperature that depends on the footpoint location within the sunspot region, with temperatures varying greatly between very closely spaced footpoint locations, even within the umbra. The X-ray loops may have the density required for free–free radio emission, but may be too hot for emission to be optically thick at such wavelengths because of the dependence of the optical depth on $T_e^{-3/2}$ (Equation (1)).

5.2. *Implications for the Emission Measure Distribution*

The proposed distribution of radio and free–free radio emission by loop system presents a plausible explanation for the derived distribution of EM. The EM measurement is only valid for optically thick free–free emission. In the previous section it was determined that free–free emission dominates at the tops of certain loops while gyroresonance is responsible for the emission near the footpoints. Since plasma transport across field lines is inhibited in the low-β corona, as these loops converge the density should increase, thus increasing the EM. The increase in EM would not be observed beyond the region along the converging loops where gyroresonance absorption takes over. The peak of the derived EM distribution would then outline the region of increasing density along the converging radio-emitting field lines where the dominating emission mechanism is still free–free. Evidence for the possibility of this configuration is found in the co-location of the converging radio loops with the EM peak, as shown in Figure 19. If this interpretation is correct, it has important consequences for studies attempting to reconcile EM values obtained from radio and X-ray observations.

6. SUMMARY AND CONCLUSIONS

One of the goals of solar microwave spectral analysis is to derive the three-dimensional arrangement of physical quantities from their observed projection onto the sky plane. In the present work we have modeled spatially and spectrally resolved microwave spectra with free–free emission, gyroresonance emission, or a stratified combination of both. The results thus obtained are used to explore relationships with observations at other wavelengths to pose a qualitative picture of the three-dimensional arrangement of the plasma above the target AR. The results of this paper are summarized as follows.

1. A revision to the algorithms implementing the CLEAN deconvolution method and the implementation of the L1 self-calibration scheme at OVSA brought the OVSA amplitudes into agreement with matching VLA data and improved the spectral continuity from brightness temperature spectra constructed from single frequency maps.
2. The joint OVSA-VLA spectra were modeled with free–free or gyroresonance emission, or a stratified combination of both where the gyroresonance component underlies the free–free emission. The two-component model was found to adequately fit spectra with a low-frequency positive slope within the uncertainties in the data. The resulting physical maps of electron temperature in both components are in agreement with previous results of co-location with the plage (free–free) or with the sunspot (gyroresonance) while imposing a vertical separation of the two layers. The derived distribution of total magnetic field from the gyroresonance component is in agreement with previous findings that the B_{tot} peak from radio observations lies at the neutral line. Additionally, our spatially resolved spectra, along with the identification of the gyroresonance layer responsible for the observed emission, allows us to derive the magnetic field and temperature distributions at the base of the corona.
3. A method is outlined for using the resulting B_{tot} maps to test the reliability of potential field extrapolations. A potential field extrapolation is tested in this manner and areas of agreement and of disagreement are identified. The areas of discrepancy are identified as regions where the radio derived B_{tot} is greater than any extrapolated magnetic field strength along those lines of sight and with regions of increased gyroresonance T_e. These regions of heightened temperature are identified with the locations of X-ray footpoints. The conclusion reached is that these X-ray footpoints are associated with regions where coronal currents raise the magnetic field strength above the potential state.

4. The association of the free–free radio component with the tops of certain loops, separate from the loops co-located with X-ray emission observed with *Hinode*'s XRT, indicate that the two loop system are different in length and the location of their footpoints. The loops associated with X-ray emission have footpoints in the penumbra while the long, radio-emitting loops are anchored in the leading portion of the umbra. Length as a proxy for radio or X-ray correlation is qualitatively ruled out because loops of similar length to that in both loop systems emerge from the center of the umbra and lie along regions where no emission is observed. Because previous studies have shown that X-ray temperatures are noticeably higher than those from radio observations, these conclusions have implications for the heating function at the base of the corona. That is, that loops emanating from above the penumbra are hotter than those from above the umbra. Previous workers have identified the need for such a configuration to explain their observations. The identification of the radio emission with certain loops produces a possible explanation for the derived distribution of EM, without which it is difficult to relate it to any other observable.

As higher quality radio data becomes available, i.e., from the expansion of OVSA currently underway (Gary et al. 2010), similar models with more complex variations in temperature can be used to fit the slight variations in those spectra. The methods outlined here can be used to iteratively arrive at an optimal magnetic field extrapolation and can constrain the values of temperature and density to be used in a full radiative-transfer calculation which would reproduce the observations if all the parameters are correct. In this manner, the full three-dimensional distribution of temperature, density, and magnetic field above ARs may be obtained directly from observations.

We thank Dr. T Bastian for the SOLCAL calibration of the VLA data and Dr. A. Vourlidas for helpful discussions on solar radio emission. This work was supported by NSF grant AST-0908344, NASA grant NNG06GJ40G and NSF GK-12 Award 0638423 to the New Jersey Institute of Technology. *SoHO* is a project of international cooperation between ESA and NASA. *Hinode* is a Japanese mission developed and launched by ISAS/JAXA, collaborating with NAOJ as a domestic partner, NASA and STFC (UK) as international partners. Scientific operation of the *Hinode* mission is conducted by the *Hinode* science team organized at ISAS/JAXA. This team mainly consists of scientists from institutes in the partner countries. Support for the post-launch operation is provided by JAXA and NAOJ (Japan), STFC (UK), NASA, ESA, and NSC (Norway).

REFERENCES

Alissandrakis, C. E. 1981, A&A, 100, 197
Alissandrakis, C. E., Gel'Frejkh, G. B., Borovik, V. N., Korzhavin, A. N., Bogod, V. M., Nindos, A., & Kundu, M. R. 1993, A&A, 270, 509
Alissandrakis, C. E., & Kundu, M. R. 1982, ApJ, 253, L49
Alissandrakis, C. E., Kundu, M. R., & Lantos, P. 1980, A&A, 82, 30
Aschwanden, M. J. 2004, Physics of the Solar Corona, An Introduction (Berlin: Springer)
Chiuderi-Drago, F., Bandiera, R., Willson, R. F., Slottje, C., Falciani, R., Antonucci, E., Lang, K. R., & Shibasaki, K. 1982, Sol. Phys., 80, 71
Chiuderi Drago, F., Felli, M., & Tofani, G. 1977, A&A, 61, 79
Cornwell, T., & Fomalont, E. B. 1999, in ASP Conf. Ser. 180, Synthesis Imaging in Radio Astronomy II, ed. G. B. Taylor, C. L. Carilli, & R. A. Perley (San Francisco, CA: ASP), 187
Delaboudinière, J.-P., et al. 1995, Sol. Phys., 162, 291
De Rosa, M. L., et al. 2009, ApJ, 696, 1780
Dulk, G. A. 1985, ARA&A, 23, 169
Dulk, G. A., & Gary, D. E. 1983, A&A, 124, 103
Felli, M., Lang, K. R., & Willson, R. F. 1981, ApJ, 247, 325
Foukal, P. V., Noyes, R. W., Reeves, E. M., Schmahl, E. J., Timothy, J. G., Vernazza, J. E., Wilhbroe, G. L., & Huber, M. C. E. 1974, ApJ, 193, L143
Gary, D. E., & Hurford, G. J. 1987, ApJ, 317, 522
Gary, D. E., & Hurford, G. J. 1994, ApJ, 420, 903
Gary, D. E., & Hurford, G. J. 2004, in Solar and Space Weather Radiophysics, ed. D. E. Gary & C. U. Keller (Boston, MA: Kluwer), 71
Gary, D. E., Hurford, G. J., Nita, G. M., Fleishman, G. D., & McTiernan, J. M. 2010, American Astronomical Society Meeting Abstracts, 216, 405.20
Gary, G. A., & Hagyard, M. J. 1990, Sol. Phys., 126, 21
Gelfreikh, G. B. 2004, in Solar and Space Weather Radiophysics, ed. D. E. Gary & C. U. Keller (Boston, MA: Kluwer), 115
Georgoulis, M. K., & LaBonte, B. J. 2007, ApJ, 671, 1034
Gopalswamy, N., White, S. M., & Kundu, M. R. 1991, ApJ, 379, 366
Hinode Solar Optical Telescope Data Analysis Guide 2009, http://hesperia.gsfc.nasa.gov/ssw/hinode/sot/doc/guide/SAGv3.3.pdf
Holt, S. S., & Ramaty, R. 1969, Sol. Phys., 8, 119
Hurford, G. J. 1986, Solar Flares and Coronal Physics Using P/OF as a Research Tool, ed. E. Tandberg-Hanssen, R. M. Wilson, & H. S. Hudson (NASA Conf. Pub. 2421; Washington, DC: NASA), 191
Kakinuma, T., & Swarup, G. 1962, ApJ, 136, 975
Katsukawa, Y., et al. 2007, PASJ, 59, 577
Kundu, M. R., Schmahl, E. J., & Rao, A. P. 1981, A&A, 94, 72
Lang, K. R., & Willson, R. F. 1980, in IAU Symp. 86, Radio Physics of the Sun, ed. M. R. Kundu & T. E. Gergely (Cambridge: Cambridge Univ. Press), 109
Lang, K. R., & Willson, R. F. 1982, ApJ, 255, L111
Lang, K. R., Willson, R. F., & Gaizauskas, V. 1983, ApJ, 267, 455
Lang, K. R., Willson, R. F., Smith, K. L., & Strong, K. T. 1987a, ApJ, 322, 1035
Lang, K. R., Willson, R. F., Smith, K. L., & Strong, K. T. 1987b, ApJ, 322, 1044
Lee, J. W., Gary, D. E., & Hurford, G. J. 1993, Sol. Phys., 144, 349
Lites, B. W., Elmore, D. F., & Streander, K. V. 2001, in ASP Conf. Proc. 236, Advanced Solar Polarimetry—Theory, Observation, and Instrumentation, ed. Michael Sigwarth (San Francisco, CA: ASP), 33
Melrose, D. B., & McPhedran, R. C. 1991, Electromagnetic Processes in Dispersive Media (Cambridge: Cambridge Univ. Press)
Metcalf, T. R., et al. 2008, Sol. Phys., 247, 269
Mok, Y., Mikić, Z., Lionello, R., & Linker, J. A. 2005, ApJ, 621, 1098
Nindos, A., Kundu, M. R., White, S. M., Shibasaki, K., & Gopalswamy, N. 2000, ApJS, 130, 485
Ramaty, R., & Petrosian, V. 1972, ApJ, 178, 241
Rosner, R., Tucker, W. H., & Vaiana, G. S. 1978, ApJ, 220, 643
Scherrer, P. H., et al. 1995, Sol. Phys., 162, 129
Schmidt, H. U. 1964, in Proc. AAS-NASA Symposium, The Physics of Solar Flares, ed. W. N. Hess (NASA Special Publication, Vol. 50; Washington, DC: NASA), 107
Schrijver, C. J., et al. 2006, Sol. Phys., 235, 161
Schrijver, C. J., et al. 2008, ApJ, 675, 1637
Schwab, F.R. 1982, Robust Solution for Antenna Gains, VLA Scientific Memorandum No. 136 (Socorro, NM: NRAO), http://www.vla.nrao.edu/memos/sci/136.pdf
Shevgaonkar, R. K., & Kundu, M. R. 1985, Sol. Phys., 98, 119
Takakura, T. 1972, Sol. Phys., 26, 151
Thompson, A. R., Clark, B. G., Wade, C. M., & Napier, P. J. 1980, ApJS, 44, 151
Vourlidas, A. 1996, PhD thesis, New Mexìco Inst. of Mining and Technology
Vourlidas, A., & Bastian, T. S. 1996, ApJ, 466, 1039
Vourlidas, A., Bastian, T. S., & Aschwanden, M. J. 1997, ApJ, 489, 403
Vourlidas, A., Bastian, T. S., Nitta, N., & Aschwanden, M. J. 1996, Sol. Phys., 163, 99
White, S. M. 2004, in Solar and Space Weather Radiophysics, ed. D. E. Gary & C. U. Keller (Boston, MA: Kluwer), 89
White, S. M., & Kundu, M. R. 1997, Sol. Phys., 174, 31
White, S. M., Kundu, M. R., & Gopalswamy, N. 1992, ApJS, 78, 599
Zheleznyakov, V. V. 1962, SvA, 6, 3
Zheleznyakov, V. V. 1970, Radio Emission of the Sun and Planets (Oxford: Pergamon)
Zlotnik, E. Y., Kundu, M. R., & White, S. M. 1996, Radiophys. Quantum Electron., 39, 255
Zlotnik, E. Y., White, S. M., & Kundu, M. R. 1998, in ASP Conf. Ser. 155, Three-dimensional Structure of Solar Active Regions, ed. C. E. Alissandrakis & B. Schmieder (San Francisco, CA: ASP), 135